

RESEARCH ARTICLE | JULY 26 2024

Development of a high performance MagLIF target platform using high aspect ratio coated liners and low-mix laser preheat

Special Collection: [Papers from the 65th Annual Meeting of the APS Division of Plasma Physics](#)

A. J. Harvey-Thompson  ; M. E. Geissel ; W. E. Lewis ; D. A. Yager-Elorriaga ; M. R. Weis ; C. A. Jennings; J. R. Fein ; D. J. Ampleford ; M. R. Gomez ; E. C. Harding ; S. B. Hansen ; D. E. Bliss ; G. A. Chandler ; G. S. Dunham ; E. S. Field ; B. R. Galloway ; M. Glinsky ; K. D. Hahn ; P. F. Knapp ; D. C. Lampa ; L. M. Lucero ; M. A. Mangan ; R. R. Paguio ; L. Perea; K. J. Peterson ; J. L. Porter ; P. K. Rambo ; G. K. Robertson; G. A. Rochau ; D. E. Ruiz ; C. L. Ruiz ; M. A. Schaeuble ; J. Schwarz ; J. E. Shores; D. B. Sinars ; S. A. Slutz ; G. E. Smith; I. C. Smith; C. S. Speas; K. Whittemore; E. P. Yu 



Phys. Plasmas 31, 072711 (2024)

<https://doi.org/10.1063/5.0201770>

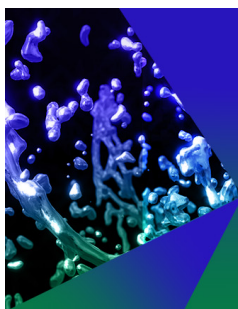


View
Online



Export
Citation



27 July 2024 16:26:07



Physics of Plasmas

Publish open access for free

[Learn More](#)

Development of a high performance MagLIF target platform using high aspect ratio coated liners and low-mix laser preheat

Cite as: Phys. Plasmas **31**, 072711 (2024); doi: 10.1063/5.0201770

Submitted: 31 January 2024 · Accepted: 23 May 2024 ·

Published Online: 26 July 2024



View Online



Export Citation



CrossMark

A. J. Harvey-Thompson,^{1,a)} M. E. Geissel,¹ W. E. Lewis,¹ D. A. Yager-Elorriaga,¹ M. R. Weis,¹ C. A. Jennings,¹ J. R. Fein,¹ D. J. Ampleford,¹ M. R. Gomez,¹ E. C. Harding,¹ S. B. Hansen,¹ D. E. Bliss,¹ G. A. Chandler,¹ G. S. Dunham,¹ E. S. Field,¹ B. R. Galloway,¹ M. Glinsky,¹ K. D. Hahn,⁵ P. F. Knapp,⁴ D. C. Lamppa,¹ L. M. Lucero,¹ M. A. Mangan,¹ R. R. Paguio,² L. Perea,¹ K. J. Peterson,¹ J. L. Porter,¹ P. K. Rambo,¹ G. K. Robertson,¹ G. A. Rochau,¹ D. E. Ruiz,¹ C. L. Ruiz,¹ M. A. Schaeuble,¹ J. Schwarz,¹ J. E. Shores,¹ D. B. Sinars,¹ S. A. Slutz,¹ G. E. Smith,² I. C. Smith,¹ C. S. Speas,¹ K. Whittemore,¹ and E. P. Yu¹

AFFILIATIONS

¹Sandia National Laboratories, P.O. Box 5800, Albuquerque, New Mexico 87185, USA

²General Atomics, San Diego, California 92121, USA

³Lawrence Livermore National Laboratory, Livermore, California 94550, USA

⁴Los Alamos National Laboratory, Los Alamos, New Mexico 87545, USA

Note: This paper is part of the Special Collection: Papers from the 65th Annual Meeting of the APS Division of Plasma Physics.

Note: Paper U11 3, Bull. Am. Phys. Soc. **68** (2023).

^{a)}Invited speaker. Author to whom correspondence should be addressed: ajharve@sandia.gov

ABSTRACT

We report on a series of Magnetized Liner Inertial Fusion (MagLIF) experiments conducted on the Z pulsed power facility that utilized high aspect ratio (ratio of outer radius to wall thickness) liners with dielectric coatings and low-mix laser preheat configurations. The liners consisted of an aspect ratio of 10.6 beryllium tube coated with 75 μm of epoxy on the outside that have been shown to maintain a better implosion stability than uncoated beryllium and have demonstrated consistent stagnation performances in previous experiments [Ampleford *et al.*, Phys. Plasmas **31**, 022703 (2024)]. Two-dimensional HYDRA simulations were used to design three different “co-injection” laser configurations, whereby a second laser is used to provide an early prepulse before the main pulse, to reduce LEH foil mix while increasing the fuel density and coupled energy. The laser preheat energy for each configuration was constrained using dedicated laser experiments before being applied to the integrated MagLIF experiments on Z. The DD neutron yield for experiments using co-injection preheat configurations is found to increase with the specific preheat energy in line with simulations. The highest neutron yield achieved in this study of 1.1×10^{13} matches the highest reported in a MagLIF experiment to date and is a factor 3.5 times higher than similar experiments using preheat with no phase plate smoothing. We attempt to assess the effects of mix and morphology to explain the improved performance; however, neither factor is found to be conclusive within the uncertainty of the measurements.

© 2024 Author(s). All article content, except where otherwise noted, is licensed under a Creative Commons Attribution (CC BY) license (<https://creativecommons.org/licenses/by/4.0/>). <https://doi.org/10.1063/5.0201770>

I. INTRODUCTION

The Magnetized Liner Inertial Fusion (MagLIF) scheme^{1,2} has successfully demonstrated significant fusion neutron yields and has a promising path to producing multi-MJ fusion yields in the future.^{3,4} Three stages are used to achieve fusion conditions at stagnation: First, the fuel is magnetized⁵ with a 10–15 T axial magnetic field to suppress radial thermal conduction; second, the fuel adiabat

is then raised by laser heating the underdense ($n_e/n_c = 0.05\text{--}0.1$) D₂ gas with the multi-kJ Z-Beamlet laser^{6,7} through inverse bremsstrahlung absorption; and finally, the fuel is compressed over ~ 60 ns with the $\sim 16\text{--}20$ MA magnetic drive supplied by the Z pulsed power generator.^{8,9} The combination of preheat, magnetization, and compression produces a hot, magnetized column of fuel at stagnation. The fuel and fusion products being magnetized relax

the density requirements for fuel self-heating¹⁰ and operate in the so-called magneto-inertial fusion regime.

Many factors play into the performance of a given MagLIF experiment, including the stability of the implosion, the preheat energy coupled to the fuel, and the amount of mix introduced into the fuel, particularly during preheat. Understanding the role of each factor across a dataset requires constraining relevant parameters, such as preheat energy, or relying on reproducible outcomes such as the stability of an implosion for a given liner design and drive history.

This study utilized the “coated AR9” liner configuration described in Ampleford *et al.*¹¹ consisting of a 10 mm tall, 4.65 mm inner diameter (I.D.) aspect ratio 10.6 (AR, ratio of outer radius to wall thickness) Be tube with a 75- μm -thick dielectric epoxy (EPON) coating on the outer surface. The liner configuration is so-called because the linear mass of the liner with the coating is equivalent to an AR9 pure Be liner and, hence, has similar implosion dynamics. The liner design was initially studied to investigate the benefits of dielectric coatings on stagnation performance in integrated targets, having been shown to effectively reduce the effects of early time electrothermal instability (ETI) growth,¹² and subsequent magneto-Rayleigh-Taylor (MRT) growth during implosions.¹³ A particularly favorable quality of the integrated MagLIF experiments performed with coated AR9 liners was their consistency in terms of neutron yield, returning DD yields within the $\pm 20\%$ uncertainty range of the measurements across three repeat experiments.¹¹ Those experiments utilized a laser preheat configuration, termed “no-DPP” because no distributed phase plate (DPP) optic was used to condition the beam spot profile. This configuration is known to couple energy inefficiently and to introduce mix material into the fuel.^{14,15} The consistent stagnation performance of the coated AR9 liner experiments makes them an ideal test bed for new laser preheat configurations that utilize improved control of the spot profile and a pulse shape tailored to increase the coupled energy and reduce mix from the laser entrance hole (LEH) foil.

In this paper, we report on an effort to develop a high performance MagLIF target that incorporates advances in preheat configurations that increase the coupled energy and reduce mix and applies them to integrated MagLIF experiments utilizing coated AR9 liners. The preheat configurations developed are shown to couple up to 1700 ± 120 J of energy into the fuel and utilize a tailored “co-injection” pulse shape to mitigate the introduction of LEH mix material into the fuel. The co-injection configurations also exhibit less beam spray than for no-DPP preheat, which may reduce mix from internal surfaces inside the target. Finally, the co-injection configurations utilize higher gas densities which simulations suggest reduce the convergence ratio at stagnation¹⁶ and impact morphology. These changes would generally be expected to improve the stagnation performance. The results show a substantially improved stagnation performance for experiments with the highest energy co-injection preheat configurations, including returning the highest DD neutron yield to date of $Y_{DD} = 1.1 \times 10^{13} \pm 20\%$ neutrons in shot z3236. A similar neutron yield has been reported previously in an uncoated MagLIF experiment but only when using a higher applied magnetic field and current drive than the experiments reported here.¹⁷ A Bayesian analysis of the results also shows that the coated AR9 implosions generate high stagnation pressures and values of the generalized Lawson parameter¹⁸ in the form expressed in Knapp *et al.*¹⁹ of 1.31 ± 0.07 Gbar and 0.062 ± 0.006 , respectively, for shot z3236. The peak neutron yield

with experiments utilizing co-injection is a factor 3.5 times higher than the equivalent experiments with no-DPP laser preheat. An analysis of the amount of mix material present at stagnation and the morphology is presented but does not show significant differences between the preheat configurations. Better understanding the effects of the different preheat configurations on MagLIF performance will likely require further experiments and better diagnosis of mix and morphology. The results suggest that MagLIF experiments utilizing coated AR9 liners may achieve higher performance in the future if more recent advances in load inductance, magnetic field,¹⁷ and preheat energy²⁰ are applied to the platform.

The paper is structured as follows: Sec. II will describe the development of new laser preheat configurations and the diagnostic techniques used to understand them. Section III will describe the results from applying the preheat configurations to integrated MagLIF experiments utilizing coated AR9 liners. Finally, Sec. IV will discuss the results of this study and the potential implications for future MagLIF work.

II. DEVELOPMENT OF HIGH-ENERGY, LOW-MIX LASER PREHEAT CONFIGURATIONS

Effectively preheating a MagLIF target requires balancing several concerns. The most crucial parameters that impact MagLIF performance are the preheat energy coupled within the imploding volume,^{1,21} and the amount of mix material introduced into the fuel during the process.^{3,22} Laser preheat seeks to couple energy into the fuel through inverse bremsstrahlung absorption of a multi-kJ laser beam. While conceptually straightforward, MagLIF laser preheat has several competing design requirements and is impacted by practical considerations of the target design illustrated later in Fig. 5. The gaseous fusion fuel within the target needs to be contained with a laser entrance hole (LEH) foil, typically a thin polyimide membrane that the laser must first penetrate and that can absorb significant laser energy and introduce mix material.¹⁴ The LEH thickness required to contain the gas is a function of gas pressure and foil diameter. The foil diameter should enable the laser beam to enter without clipping, and the beam diameter should enable the energy in the laser to be deposited within the target length. Laser plasma instabilities (LPI's) are an additional concern that arises at high spot intensities. Designing MagLIF preheat, therefore, needs to balance the desire to utilize large spot sizes to reduce beam intensity and absorb more energy within the target length and the benefits of smaller diameter, thinner LEH foils. We note that recent advances in MagLIF target designs²⁰ have enabled a robust, cryogenically cooled platform to be fielded that addresses this tradeoff by reducing the fuel pressure within the target enabling thinner LEH foils. Testing has shown that the coated liners described in this paper are not compatible with cryogenic cooling due to cracking of the epon resin that comprises the liner coating during cooldown, so the experiments described in this paper were conducted at room temperature. This study combines experiments and diagnostic techniques to understand the coupled energy, LPI backscatter, and mix during the preheat stage with guidance from 2D simulations using the magneto hydrodynamics code HYDRA²³ to develop a series of new preheat configurations. A summary of the preheat configurations developed is given in Table I.

Examples of the temporal laser power profiles for the preheat configurations described in this paper are shown in Fig. 1. Initial coated AR9 MagLIF experiments utilized the so-called “no-DPP”

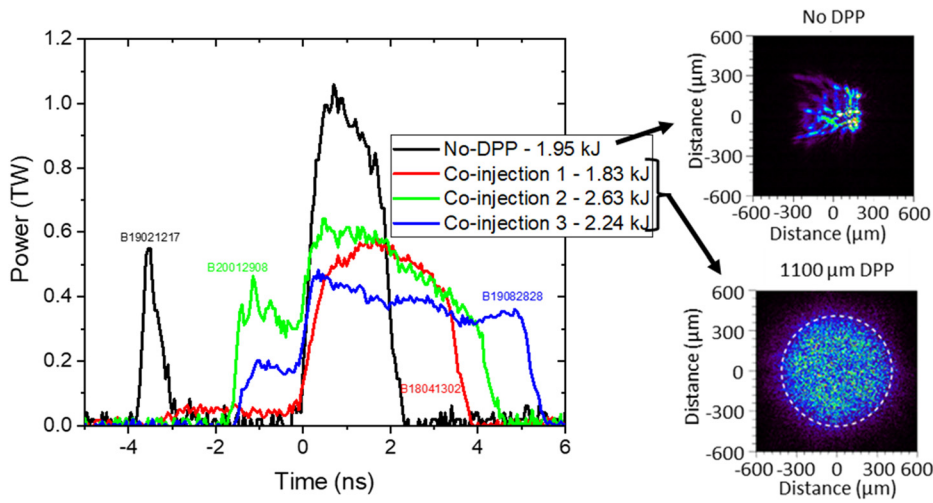


FIG. 1. Examples of pulse shapes used for the four different preheat configurations in this paper. The configuration name and energy delivered to the target are noted in the legend. Details of the ~ 20 J co-injection pulse that occurs at ~ -20 ns for the co-injection configurations are given in Ref. 14. Representative images of the spatial spot profile with and without phase plate smoothing are shown on the right.

preheat configuration, where the output of ZBL was focused ~ 3.5 mm above the LEH foil with no smoothing optics producing a non-uniform spot on the LEH foil, as shown in Fig. 1. The pulse shape utilized a ~ 300 J prepulse ~ 3.5 ns before the start of the ~ 1 TW, 1.7 kJ main pulse. The co-injection configurations all use phase plate smoothing to produce an $1100 \mu\text{m}$ diameter spot on the target, as shown in Fig. 1 and a so-called co-injection prepulse that is supplied by a second laser (Z-Petawatt)²⁴ injected along the same beamline as ZBL. This enables a low energy ($\sim 23\text{--}36$ J, 527 nm) prepulse to be delivered ~ 20 ns before the main pulse to help lower the density of the LEH foil material prior to the arrival of the main pulse and has been shown to effectively mitigate LEH foil mix.¹⁴ The development of these pulse shapes was based on several competing concerns regarding LPI backscatter, beam spray, energy deposition, penetration depth, and LEH foil mix, which were constrained using a variety of diagnostic inferences.

The preheat configurations were tested in laser-only gas cell experiments in the Pecos target chamber that has good surrogacy with the Z target chamber.^{15,25} The primary measurement in these experiments is a series of time-gated shadowgraphy images. Examples of images taken for the four pulse shapes in Fig. 1 immediately after the end of the laser pulse are shown in Fig. 2. At this time, the shadowgraphy diagnostic observes the boundary of the plasma formed by energy deposition into the gas. This boundary gives a nominal bound of where laser energy is being directly deposited into the gas and can indicate the extent to which beam spray (whereby energy in the beam is directed radially due to filamentary instabilities or other processes) is

occurring based on the radial extent of the plasma formed. Figure 2 also shows where the inner surface boundary of a MagLIF target would be in an integrated experiment. These features are described in more detail in Sec. III. All internal fuel facing surfaces (except for the LEH foil) are made from Be, which may be mixed into the fuel if directly illuminated by the laser. Evidence of mix from the cushion features^{14,26} and liner walls²⁷ has been observed previously. Also, in the case of the imploding liner, direct laser illumination may perturb the inner surface and impact instability growth.

Shadowgraphy images taken between 20 and 80 ns after the laser pulse show an expanding blast wave generated by the deposited energy. The blast wave radius can be related to the energy deposited per length into the gas at that axial location using the technique described in Harvey-Thompson *et al.*¹⁵ For each preheat configuration described, several Pecos experiments were conducted, which assessed the total energy deposited into the gas as a function of energy delivered by the laser, as shown in Fig. 3. For these experiments, the energy was changed by altering the power of the main pulse but keeping similar prepulse and foot-pulse energies. To quantify the best fit and uncertainty in the deposited energy, a Bayesian analysis of the data was conducted, shown as the shaded regions in Fig. 3, with the constraint that the deposited energy varied linearly with the energy delivered and had a constant uncertainty across the energy range. We note that this assumption about the energy deposited varying linearly with the energy delivered has been used elsewhere, e.g., Ref. 20. Due to a limited dataset, this analysis was performed by grouping the phase plate smoothed laser configurations that used a $1.77 \mu\text{m}$ thick LEH foil

TABLE I. Target parameters for the preheat configurations discussed in this paper.

Preheat config.	Gas density (mg/cc)	LEH diameter (mm)	LEH thickness (μm)	Spot diameter (μm)	Peak intensity (TW/cm^2)	SBS backscatter energy (J)
No-DPP	0.7	3	1.77	~ 500 (square)	~ 400	429
Co-injection 1	1.1	2	1.77	1100	65	42
Co-injection 2	1.1	2.2	1.77	1100	70	7
Co-injection 3	1.4	2.2	1.58	1100	60	27

together (the red points in Fig. 3). This includes the “configuration A” pulse shape described in Harvey-Thompson *et al.*¹⁴ and the “co-injection 1” and “co-injection 2” configurations described in this paper. All three configurations show similar trends in the fraction of incident energy coupled, interact with the same mass of LEH foil material, and exhibit similar, low levels of SBS backscatter.

A final piece of data that informed the development of the preheat configurations came from simulated and experimental inferences of the amount of LEH foil material driven into the fuel during preheat. The spectra in Fig. 4(b) show emission from a 1-nm cobalt coating placed on the underside (fuel-facing side) of the LEH foil in integrated experiments. The cobalt emits K shell x-rays at stagnation that are imaged with the XRS3 axially resolved crystal spectrometer.²⁸ Because the Co is applied as a coating, the technique gives a measurement of the extent of the LEH foil mix at the time of stagnation¹⁴ but not the quantity. Details of the integrated experiments will be discussed further in Sec. III, but the pulse shapes used were similar to the canonical pulse shapes described in this section and shown in Fig. 1. Figure 4(a) also shows the LEH foil mass mixed into the fuel as a function of time from 2D HYDRA simulations for the co-injection configurations. We note that simulated foil masses for the no-DPP configuration are not included due to the difficulty in simulating the spot profile accurately as described in Ref. 14. Previous work has shown that HYDRA simulations can capture trends in LEH foil mix, and so such simulations can be used to guide the development of preheat configurations that minimize this mix by tailoring the laser pulse shape, particularly the pre-pulse and foot-pulse.¹⁴ The simulations show similar trends for all preheat configurations. As discussed in Ref. 14, the interaction with the laser initially pushes foil material downwards into the imploding region of the liner. As the implosion proceeds, some of the fuel, and any material mix entrained, is ejected out the ends of the imploding region. This reduces the fuel and foil mass present as the implosion proceeds.

Combining these diagnostic techniques (plasma extent and energy deposition from shadowgraphy, SBS backscatter energy measurements, and mix from spectroscopy in integrated experiments) allows the efficacy of preheat configurations to be assessed. Initial integrated MagLIF experiments investigating coated AR9 liners utilized the no-DPP preheat configuration, which had several undesirable qualities. The spot profile, shown in Fig. 1, utilized no phase plate smoothing and may vary from shot to shot depending on the condition of the upstream optics. The nonuniformity makes the spot very challenging to simulate and cannot be adequately captured with 2D models. The spot profile includes regions with a very high intensity, which results in substantial SBS backscatter of $\sim 40\%$ at the higher energies.²⁵ It is partially because of these backscatter losses that the preheat configuration coupled energy inefficiently. For incident energies between 1.3 and 2.5 kJ, only 31.9%–45.4% of the incident energy is coupled into the gas. In some shots, significant beam spray occurs. Figure 2 shows that in shot B19021217, energy is deposited at approximately the radius of the liner for the majority of the liner length, so direct illumination of the liner walls may occur in an actual MagLIF target resulting in mix. Shot B19021217 also exhibits a bifurcation of the beam into two separate filaments. These behaviors vary shot to shot, impact the propagation depth, and may result in significant mix from the interior surfaces being introduced into the fuel. Evidence of mix material from the LEH foil is also apparent from the presence of cobalt K-shell lines in axially resolved spectra in Fig. 4(b).

Resolving these issues requires first controlling the spot profile to reduce shot-to-shot variations and create a more uniform spot envelope that can be simulated more effectively. As shown in Table I, all co-injection preheat configurations tested used a DPP optic to produce an $1100\text{ }\mu\text{m}$ diameter super-Gaussian spot profile, as illustrated in Fig. 1. This, combined with a reduction in peak power to $\sim 0.6\text{--}0.7\text{ TW}$, significantly reduced the peak intensity to below $70\text{ TW}/\text{cm}^2$ for all co-injection configurations and effectively mitigated SBS

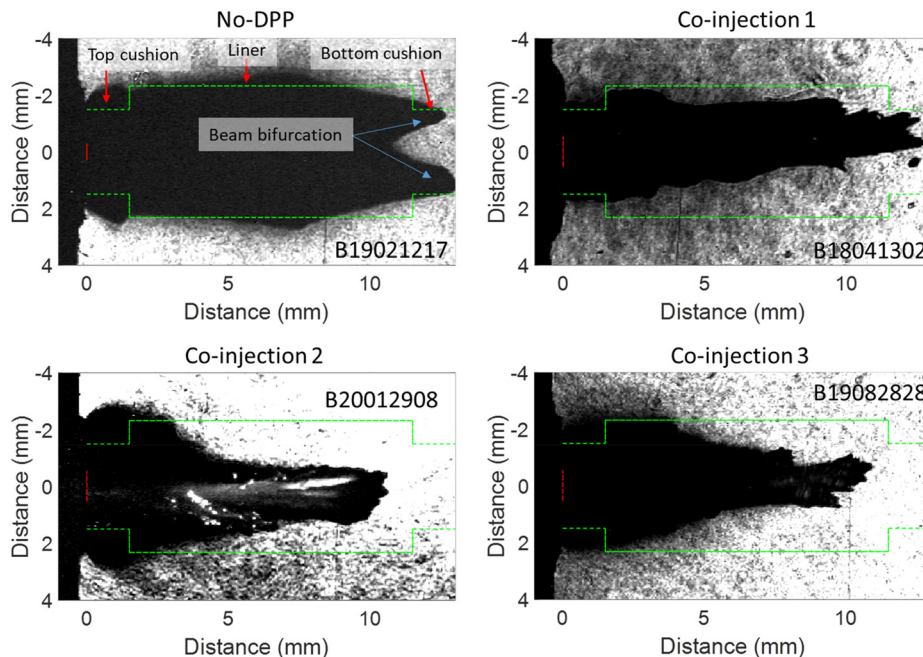


FIG. 2. Shadowgraphy images taken $<1\text{ ns}$ after the end of the main pulse for the different preheat configurations described in this paper. The specific shots represented utilized the pulse shapes shown in Fig. 1. The initial location of the LEH before pressurization is at $x=0$, $y=0$ in each image. The red dashed line to the left represents the initial spot size of the laser that interacts with the LEH foil. The green dashed lines represent where the internal surfaces of an integrated MagLIF target would be in these images.

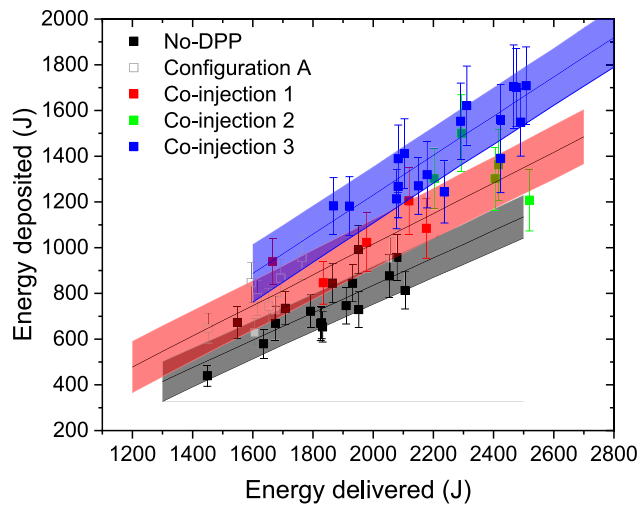


FIG. 3. The energy deposited into the gas vs energy delivered by the laser for different preheat configurations described in this paper as inferred from shadowgraphy images in Pecos experiments. Each point represents an individual Pecos experiment. The solid lines and shaded regions represent the best linear fit to these data and the uncertainty as calculated from a Bayesian analysis. The configuration A, co-injection 1, and co-injection 2 configurations were treated as belonging to the same dataset for this purpose to gain better statistics over a large energy range.

backscatter to $<5\%$ in line with previous studies.²⁵ We note though that losses to SRS backscatter were not well constrained in the experiments. All the co-injection configurations also exhibit less beam spray, indicated by the plasma being generated at a smaller radius along the liner than the no-DPP configuration. This may lead to less material mix being introduced from the liner walls, although energy is still deposited at the top cushion location so material mix from this feature may be similar.

The co-injection 1 configuration introduced a co-injection pre-pulse and a long, low power foot pulse and increased the gas density to 1.05 mg/cm^3 based on 2D HYDRA simulations, which suggested LEH foil mix should be effectively mitigated. This result was confirmed experimentally as shown in Fig. 4(b). Despite the increased gas density and pressure, the target maintained a $1.77\text{-}\mu\text{m}$ thick LEH foil, which was achieved by reducing the foil diameter from 3 to 2 mm. The co-injection 1 and co-injection 2 configurations effectively increased the coupling efficiency to 39.8% – 55% for incident energies between 1.2 and 2.7 kJ, respectively, despite the larger spot size beam interacting with more LEH foil material. Overall, the co-injection 1 configuration increased coupling efficiency, mitigated LEH foil mix, and produced a more consistent heating of the plasma with reduced beam spray as shown in Fig. 2.

While the co-injection 1 configuration successfully reduced LEH foil mix, the energy coupled into the gas was limited by the low energy delivered by the laser to a maximum $\sim 1 \text{ kJ}$ in experiments. This energy limitation arises because ZBL is poorly optimized to produce long, low-power pulse shapes and does not efficiently convert energy from the amplifier stages into 2ω light at low powers. To enable higher energies, the co-injection 2 pulse shape shortened the foot pulse length to $\sim 1 \text{ ns}$, as shown in Fig. 1, enabling the main pulse to be extended to 4.5 ns with more energy. Other parameters, including the co-injection

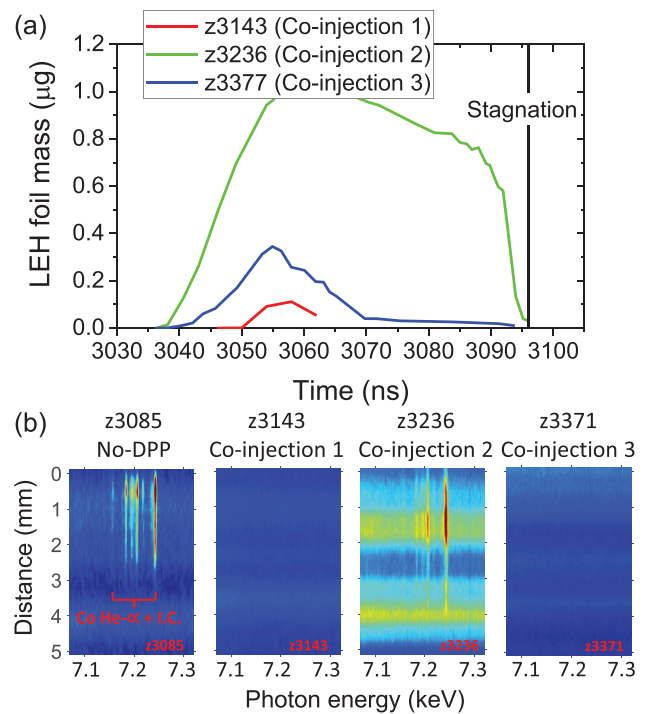


FIG. 4. (a) Simulated masses of LEH foil material mixed into the fuel in the imploding region of the liner vs time taken from 2D HYDRA simulations for the different co-injection configurations. The simulated mix for the no-DPP configuration is not presented due to the difficulty of modeling that configuration.¹⁴ The axially resolved spectral data covering the Co He- α and intercombination (I.C.) lines for experiments utilizing each preheat configuration are shown in (b). Each experiment shown utilized a 1 nm Co coating on the underside (fuel-facing side) of the LEH foil. Shot z3085 used an uncoated AR6 liner, but the mix dynamics are thought to be similar to the coated AR9 liners that are the focus of this paper. An arbitrary intensity scale is used so the axial extent of cobalt emission can be clearly seen. The data show that the co-injection 2 configuration has LEH foil mix remaining in the stagnation column, while the co-injection 1 and 3 configurations do not in line with simulations.

pulse, were kept the same as the co-injection 1 configuration. The LEH foil remained $1.77 \mu\text{m}$ thick, but the diameter was increased to 2.2 mm to prevent potential clipping of the beam on the washer. The higher energies enabled up to $\sim 1.4 \text{ kJ}$ energy coupled to the fuel and a coupled specific preheat energy (energy per mass of fuel) of up to 7.8 kJ/mg , which is thought to be close to the optimum, as discussed in Sec. III. As shown in Fig. 4, experimental data and post-shot simulations showed that some LEH foil material was again pushed into the imploding fuel volume and remains for the duration of the implosion. Simulations suggest this is due to the shorter, higher power foot pulse and subsequent main pulse imparting energy to the foil material more rapidly before the foil material heats and becomes underdense. As discussed in Ref. 14, the downward motion of the foil is sensitive to the pressure balance between the fuel and LEH foil material, which is impacted by these early time energetics. Based on the simulations shown in Fig. 6, the peak simulated LEH foil mass ($\sim 1 \mu\text{g}$) is likely sufficient to impact the yield.

The next iteration of preheat design, co-injection 3, increased the D_2 fuel density to 1.4 mg/cc (120 psi). This was motivated by 2D

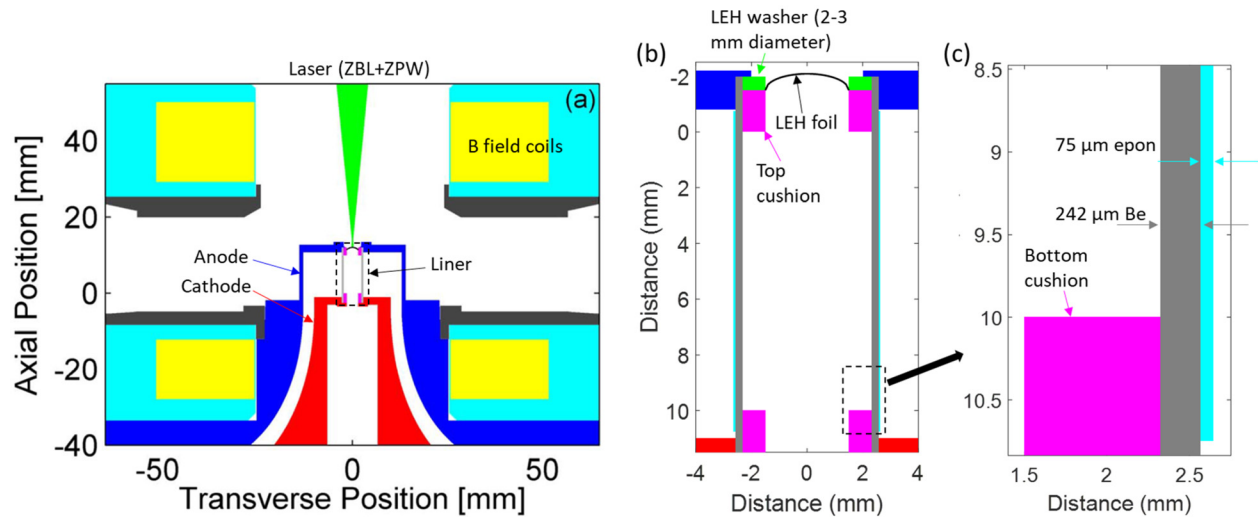


FIG. 5. (a) Cross section of the experimental load region illustrating the magnetic field coils and final transmission lines in the Z chamber, adapted with permission from Gomez *et al.*, Phys. Rev. Lett. **125**(15), 155002 (2020); licensed under a Creative Commons Attribution (CC BY) license. Detailed illustrations of the liner geometry are shown in (b) and (c) adapted with permission from Ampleford *et al.*, Phys. Plasmas **31**(2), 022703 (2024); licensed under a Creative Commons Attribution (CC BY) license.

HYDRA simulations that indicated less foil material would be injected into the fuel as shown in Fig. 4(a), and by a predicted reduction in the stagnation convergence ratio afforded by higher fuel densities.¹⁶ The LEH parameters for co-injection 3 were also adjusted, utilizing a 2.2 mm diameter 1.58 μm thick foil despite the higher fuel density. This reduction in the foil thickness was made possible by improved testing procedures that increased our confidence in placing greater strains on the LEH foil material. As shown in Fig. 1, the laser pulse shape contained a similar energy to the high-energy co-injection configuration (~ 2.5 kJ) but with a longer, lower-power main pulse. The co-injection 3 configuration coupled energy more efficiently into the fuel, coupling 55.0%–69.7% for incident energies between 1.6 and 3.0 kJ. Despite this, the higher fuel density meant the maximum specific energy coupled was slightly lower than for the co-injection 2 configuration reaching 7.1 kJ/mg for 1.7 kJ preheat energy coupled. As shown in Fig. 4(b), LEH mix was not observed at stagnation for the co-injection 3 configuration in line with simulation predictions.

III. INTEGRATED TARGET PERFORMANCE

The integrated MagLIF experiments described in this paper all utilized a similar experimental setup with the primary difference being the preheat parameters. The liners used the “coated AR9” geometry described in Ampleford *et al.*¹¹ and illustrated in Fig. 5 coupled to a high inductance (7.4 nH) final transmission line and load region. The liners consist of a Be tube with a 4.65 mm I.D. and 5.134 mm outer diameter (O.D.) with a 75 μm thick dielectric (epon) coating on the O.D. A washer is located within the tube that holds the LEH foil whose thickness and aperture diameter are dependent on the preheat configuration as described in Sec. II. Beneath the washer is a 1.5 mm tall, 3 mm I.D. Be “cushion,” followed by a 10 mm long imploding region that has no internal components, and finally, a second 3 mm I.D. Be cushion at the bottom. The liner is placed in an extended transmission line that allows room for two magnetic field coils to supply a 10 T axial magnetic field to the target volume.⁵ The overall geometry has been

applied previously to many integrated MagLIF experiments. All experiments used a D_2 gas fill with initial densities that varied with the preheat configuration as described in Sec. II and listed in Table I. Some experiments (z3180, z3269, z3371, and z3377) had 3.0–3.6 ppm Kr dopant included in the gas for diagnostic purposes that is not thought to significantly impact the stagnation conditions discussed.

A. Summary of stagnation conditions

Each experiment used a similar suite of diagnostics to constrain the stagnation parameters using the Bayesian approach outlined in Knapp *et al.*¹⁹ The x-ray emission was constrained in various energy bins using a series of filtered diodes for time resolution and with the TIPC filtered pinhole imager²⁹ for axial spatial resolution. The volume of the stagnated plasma was determined using different configurations of the spherical crystal imager (SCI) diagnostic³⁰ that provides high-resolution images whose details will be given in Sec. III B. The SCI was not fielded in shot z3377 and so the TIPC data were used to provide a less-constraining prior on the volume in that shot. The DD neutron yield was measured with a series of indium activation samples. The neutron spectrum was measured with both side-on and end-on neutron time of flight (NTOF) detectors,^{31,32} from which the ion temperature and values of the magnetic field-radius product, BR,³³ were inferred. However, the axial NTOFS did not return good data on the final four shots so values of BR could not be reliably calculated for those shots. For this reason, we do not explore trends in BR in this paper, but note a more thorough analysis of BR that includes this and other datasets is presented in Ref. 33. A summary of the stagnation conditions inferred based on these diagnostics is shown in Table II.

Figure 6(a) plots the neutron yields as a function of specific energy deposited into the fuel for different preheat configurations taken from data in Table II. Figure 6(a) also shows the yield as a function of specific energy from 2D simulations using the radiation Magnetohydrodynamics code Kraken (a derivative of the code

Gorgon)^{34,35} with different fuel densities. The simulations assume an AR9 pure Be liner with no dielectric coating and no instability growth, and that preheat energy is deposited uniformly along the imploding length of the liner. These “2D clean” simulations used a similar set of assumptions to previous Lasnex simulations that have investigated various MagLIF scalings and dependencies.^{3,16} The simulations and similarity scaling theory^{21,36} suggest that the neutron yield varies similarly with specific energy for different fuel densities, allowing the relative performance of different preheat configurations to be compared on this plot. Figure 6(a) also shows the effect of polyimide foil mix on the neutron yield for the 0.7 mg/cc gas fill in 2D Kraken simulations. Introducing mix lowers the peak predicted neutron yield and increases the preheat energy required to maximize that yield.

Experiments using the “no-DPP” preheat configuration coupled 7.9–8.4 kJ/mg preheat energy into the fuel and returned consistent neutron yields of $Y_{DD} = 2.6\text{--}3.1 \times 10^{12}$. The dataset using co-injection configurations exhibits a significantly different trend in the yield, which increases from $Y_{DD} = 1.3\text{--}11 \times 10^{12}$ over the range of specific coupled energies from 4.0 to 7.8 kJ/mg. The highest neutron yield, $Y_{DD} = 11 \times 10^{12}$ (z3236), is a factor ~ 4 higher than for the no-DPP preheat configuration. Shot z3299 is an outlier with respect to these trends, returning $Y_{DD} = 2.3 \times 10^{12}$ while depositing 8.1 kJ/mg preheat energy. However, on this experiment, time-gated cameras observing the LEH foil detected particles of debris above the target interacting with the preheat laser. This may have reduced the deposited energy; however, we cannot currently quantify the effect. We note that only two other shots in this dataset, z3236 and z3371, utilized axial cameras, and we did not observe debris on those shots. Debris on other shots that did not field axial cameras cannot be ruled out.

The generalized Lawson parameter, χ , measures the ratio of the energy deposited by 3.5 MeV alpha particles created by DT reactions to the internal energy of the fuel, with $\chi > 1$ being a necessary condition for ignition.¹⁸ We follow the expression for χ in Knapp *et al.*¹⁹ as $\chi = \frac{2}{3} \frac{f_D f_T}{(1+\langle Z \rangle)^2} \frac{\epsilon_\alpha}{V_{HS}} \int_V P_{HS} \frac{\langle \sigma v \rangle_{DT}}{T^2} dV$, where $\epsilon_\alpha = 3.5$ MeV is the energy of a DT fusion α -particle, $f_{D(T)}$ is the fraction of deuterium (tritium) in the fuel, $\langle \sigma v \rangle_{DT}$ is the (ion temperature-dependent) DT fusion reactivity, P_{HS} is the hotspot pressure, T is the fuel temperature, τ is the burn duration, V_{HS} is the hotspot volume, and $\langle Z \rangle$ is the average ionization. Values of the generalized Lawson parameter, χ , are computed based on a Bayesian analysis of the data as described in Knapp *et al.*,¹⁹ listed in Table II, and plotted in Figs. 7(a) and 7(b). The data show a similar trend in values of χ as in the neutron yield. For the co-injection configurations, χ increases with specific preheat energy from 0.013 ± 0.002 for z3180 to 0.062 ± 0.006 for z3236, with z3299, where preheat may have been compromised by debris, being an outlier. Again, experiments with the no-DPP configuration produced relatively consistent values of χ between 0.019 ± 0.003 and 0.029 ± 0.003 but were significantly outperformed by the best co-injection shots. We note the large uncertainty in χ for z3377 is due to there being no data from the SCI on that shot to constrain the hotspot volume. The value of χ for z3236 and z3377 compares favorably with the best-performing shots in the MagLIF dataset, especially given that more recent MagLIF experiments have improved the input parameters (current, preheat energy, and magnetic field) further in uncoated MagLIF experiments.

As shown in Fig. 7(b), the factor that most strongly correlates with the value of χ across the dataset is the ion temperature. Similarly, the neutron yield generally shows a strong correlation with ion

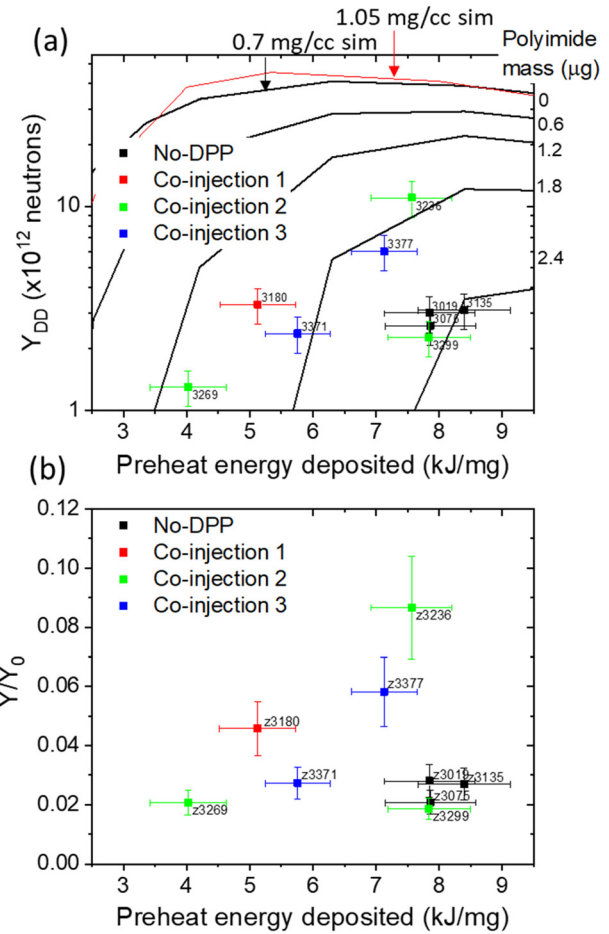


FIG. 6. (a) Neutron yields as a function of specific deposited energy for MagLIF shots using different preheat configurations. Also plotted are 2D Kraken simulations for 0.7 (black) and 1.05 mg/cc (red) fuel densities, demonstrating that the performance is expected to scale similarly with specific preheat energy at different fuel densities. The results from 2D Kraken simulations for a 0.7 mg/cc fuel that has different masses of polyimide mixed atomically into the fuel at the time of preheat are also shown to illustrate the effect that mix has on performance. The measured neutron yield divided by the yield from 2D Hydra simulations is shown in (b).

temperature as shown in Fig. 8, as expected for ion temperatures in the 2–3 keV range. Previous work¹⁷ has shown that MagLIF experiments utilizing AR6 liners follow the DD-3He fusion reactivity curve [Eq. (160) in Ref. 37] scaled by 3.9×10^{38} , shown as the AR6 scaling curve in Fig. 8. The results generally follow that trend with some variation in the dataset. The correlations point to differences in performance being chiefly driven by the ion temperature at stagnation rather than, for example, the amount of fuel participating or the burn duration.

Two factors that impact the ion temperature at stagnation are the specific preheat energy coupled and the amount of mix within the fuel volume. Figure 7(c) shows the inferred ion temperature as a function of specific preheat energy. While the dataset as a whole does not show a strong correlation, the co-injection shots show a positive correlation with z3299 being an outlier. As shown in Fig. 6(a), when the dataset is taken as a whole, there is only a weak correlation between neutron

TABLE II. The parameters of integrated MagLIF experiments discussed in this paper. The DD neutron yield (Y_{DD}) is measured using activation detectors. The filtered x-ray yield (Y_r) is measured using a silicon diode filtered with $125 \mu\text{m}$ Zn. The ion temperature (T_i) is measured by using neutron time of flight detectors. Values of the mix percentage and chi are taken from a Bayesian analysis of the data that incorporate multiple measurements. Values of the DD neutron yield divided by results of 2D Hydra simulations are shown as Y/Y_0 .

Z Shot #	Preheat config.	Coupled energy (J)	Specific energy (kJ/mg)	Y_{DD} ($\pm 20\%$) $\times 10^{12}$	Mix (Be, %)	T_i ($\pm 20\%$ keV)	Pressure (Gbar)	Chi	Instability metric ($\times 10^{-3}$)	Y/Y_0
3019	No-DPP	934 ± 85	7.9 ± 0.7	3	2.0 ± 1.2	2.27 ± 0.09	1.07 ± 0.10	0.029 ± 0.003	1.1	0.028
3075	No-DPP	935 ± 85	7.9 ± 0.8	2.6	1.7 ± 1.3	2.10 ± 0.09	1.12 ± 0.12	0.019 ± 0.003	3.6	0.021
3135	No-DPP	999 ± 87	8.4 ± 0.7	3.1	2.4 ± 1.5	2.47 ± 0.09	0.85 ± 0.07	0.027 ± 0.003	0.8	0.027
3180	Co-inj. 1	915 ± 108	5.1 ± 0.6	3.3	2.5 ± 1.6	2.06 ± 0.09	1.69 ± 0.15	0.013 ± 0.002	3.0	0.046
3236	Co-inj. 2	1350 ± 114	7.6 ± 0.6	11	2.5 ± 1.4	2.89 ± 0.10	1.31 ± 0.07	0.062 ± 0.006	3.9	0.097
3269	Co-inj. 2	719 ± 108	4.0 ± 0.6	1.3	3.0 ± 1.6	2.30 ± 0.15	1.12 ± 0.09	0.026 ± 0.004	0.2	0.021
3299	Co-inj. 2	1399 ± 117	7.8 ± 0.7	2.28	1.9 ± 1.3	2.03 ± 0.08	1.16 ± 0.10	0.015 ± 0.002	1.0	0.019
3371	Co-inj. 3	1371 ± 122	5.8 ± 0.5	2.38	1.0 ± 1.0	2.53 ± 0.19	0.95 ± 0.09	0.037 ± 0.007	3.0	0.027
3377	Co-inj. 3	1696 ± 124	7.1 ± 0.5	6	1.2 ± 1.2	2.79 ± 0.15	1.24 ± 0.32	0.056 ± 0.018	N/A	0.058

yield and specific preheat energy. However, the correlation for co-injection experiments is much stronger, with z3299 again being an outlier. A similar trend can be found when comparing yields to 2D clean Hydra simulations that make similar assumptions about instability growth, preheat, and liner composition as the 2D clean Kraken simulations described earlier in this section. The ratio of measured neutron yield to these simulations, Y/Y_0 , is given in Table II and plotted in Fig. 6(b). The comparison shows again that experiments utilizing co-injection preheat configurations achieve higher values of Y/Y_0 for comparable specific preheat energies, and that Y/Y_0 trends higher with increased specific preheat energy among co-injection shots. A possible explanation for these observations is that the co-injection experiments are introducing less mix than the no-DPP experiments and so achieve higher yields and values of χ for a given specific preheat energy. Mix might also explain details of the positive trends in Y/Y_0 with specific preheat energy for the co-injection shots as mix material in the fuel tends to increase the specific preheat energy required to maximize yield as illustrated by the Kraken simulations in Fig. 6(a). Differences in LEH mix material between co-injection configurations shown in Figs. 4(a) and 4(b) do not appear to have a significant effect within the co-injection dataset however. For example, the co-injection 1 experiment (z3180) follows the same trend in neutron yield with preheat energy and even underperforms the co-injection 2 experiments by the metrics in Fig. 7 despite exhibiting less LEH foil mix. This might point to LEH foil mix being relatively unimportant generally or it being one of several factors that vary between notionally similar experiments.

Figure 8 shows the percentage of material mix within the fuel at stagnation, assuming the mix material is beryllium, calculated by the Bayesian analysis. This analysis, however, does not constrain mix between the different preheat configurations sufficiently to conclude that mix explains differences in performance between the co-injection and no-DPP configurations. For example, varying the percentage of Be mix introduced at the time of preheat from 1% to 3% (approximately the range of uncertainty for the no-DPP shots) reduces the yield by a factor 2.5–20 based on 2D LASNEX simulations.¹⁶ If mix is playing a significant role in the observed trends, it is important that better diagnostic techniques be developed in the future to quantify its impact.

B. Stagnation morphology

Another factor that is expected to significantly impact the stagnation performance and that may be affected by the co-injection preheat configurations is stability. Instability growth during MagLIF implosions can impact the compression and confinement of the fuel and introduce contaminants and variability. While the application of dielectric coatings was shown to improve the stagnation morphology compared to equivalent uncoated AR9 Be liner implosions,¹¹ the stagnation morphology is still clearly impacted by instability growth and shows 3D structures not captured in 2D simulations. The development of instabilities can lead to shot-to-shot variations in the overall compression of the column, and it is possible that the impact of instabilities may dominate performance over other factors such as preheat energy and preheat-induced mix. The co-injection experiments here varied the preheat energy deposited and utilized higher density gas fills. In 2D simulations, the higher fill density and higher preheat energy coupled are observed to modestly reduce the stagnation convergence ratio,¹⁶ which may impact morphology.

The primary diagnostic that characterized the stagnation morphology in these experiments was different implementations of SCIs³⁰ that observed the stagnation emission. All co-injection shots used the High-Resolution Continuum x-ray Imager (HRCXI) that achieves a $15 \times 16 \mu\text{m}$ (horizontal by vertical) spatial resolution and observes x-rays in narrow bands primarily at 6.21 and 9.32 keV. The no-DPP shots used a variety of other crystal configurations described in Harding *et al.*³⁰ Shot z3019 used the continuum x-ray imager (6.2 and 9.4 keV, $59 \times 83 \mu\text{m}$ horizontal by vertical resolution), z3135 used the Iron He- β imager (continuum channel, 7.9 keV, $63 \times 66 \mu\text{m}$ horizontal by vertical resolution), and z3075 used the Iron K α 1 imager (continuum channel, 6.4 keV, $64 \times 66 \mu\text{m}$ horizontal by vertical resolution).

The data from the SCI diagnostics are shown in Fig. 9. Shot z3377 did not field a crystal imager, and so no data were collected. The data show a range of structures appearing across the dataset including separated strands of emission (bifurcations), axial variations in intensity, and variations in the mean radial position of the column.

While more advanced techniques are being developed to better quantify the stagnation morphology, we follow Ampleford *et al.*,¹¹

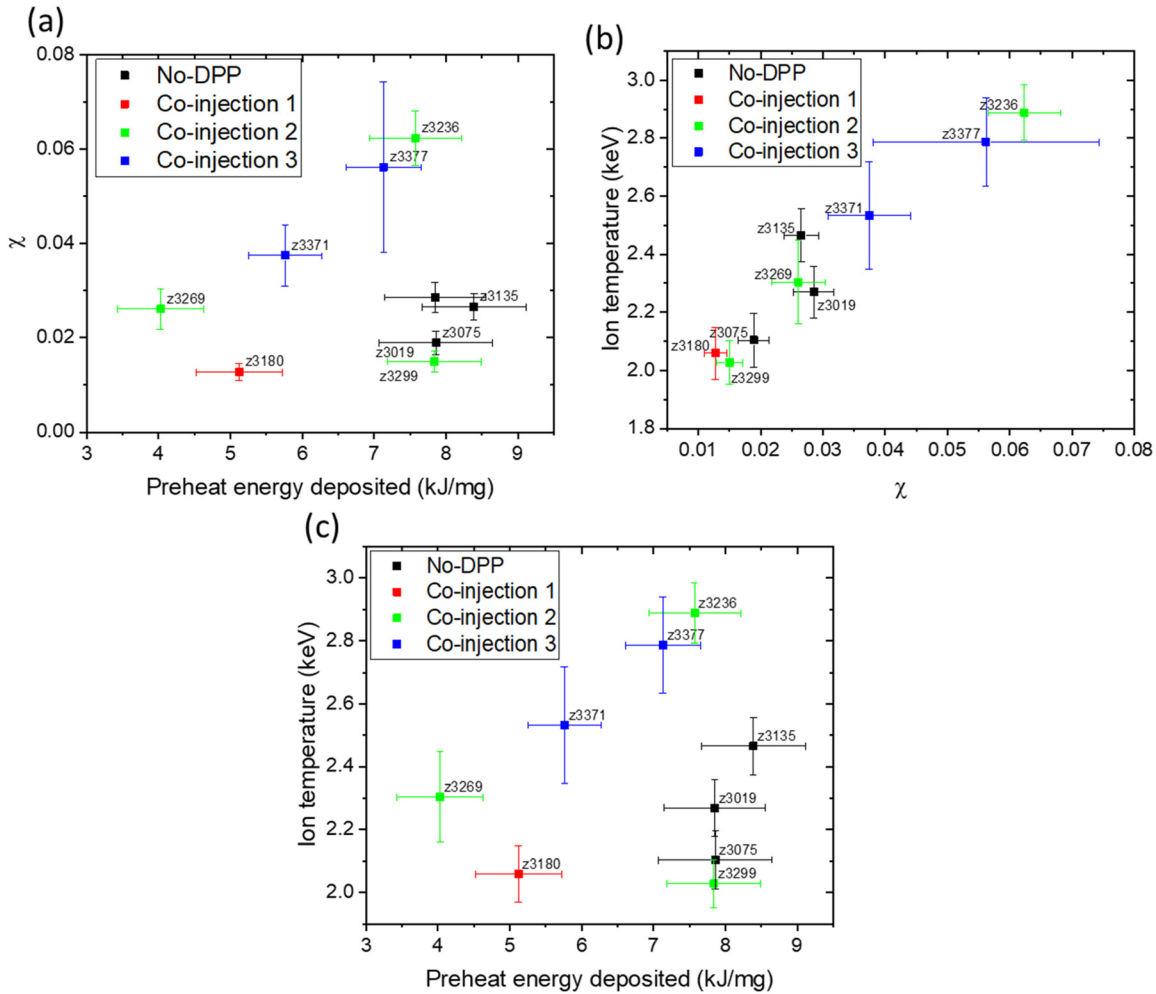


FIG. 7. The value of the generalized Lawson parameter, χ , for the experiments as determined from a Bayesian analysis of the stagnation data as a function of (a) the specific preheat energy and (b) the ion temperature. The ion temperature as a function of preheat energy is shown in (c).

utilizing the integral of the power spectrum from a Fourier transform of the column’s mean radial position vs height, as a measurement of total instability. Larger values of this integral, $\int |\hat{f}(k)|^2 dk$, correspond to more unstable columns due to larger amplitude variations in the radial position of the stagnation column. This is indicative of the feed-through of instabilities, which are exacerbated during the deceleration of the liner against the hot fuel and can limit compression and introduce mix. Figure 9 shows the inferred mean radial positions (overlaid as green lines in each image) that are obtained as follows. For each axial slice, the left and right positions are tracked by identifying the left-most and right-most horizontal positions that match the 10% value of the maximum intensity within that slice. Then, these left and right positions are averaged, equaling the “mean radial position” of the column. Although slightly different than the characterization of strand position used in Ampleford *et al.*, in practice, the final traces are very similar with the mean radial position better matching the overall shape of the column in bifurcated regions, where the emission profile is poorly approximated by a Gaussian distribution. We re-computed the

instability metric for the experiments in Ampleford *et al.* using the mean radial position instead of the Gaussian centroid position. For reference, the uncoated AR6 experiments had values of 0.006 (z2839) and 0.004 (z2979) mm³, whereas the uncoated AR9 experiments had higher values of 0.007 (z3018) and 0.008 (z3303) mm³. The coated “No-DPP” AR9 experiments in Ampleford *et al.*¹¹ are included as part of the main dataset in this work and shown in Fig. 10. We note the lower resolution of the SCIs used for the no-DPP experiments may reduce the relative value of the instability metric compared to the co-injection shots by ~12% but that does not alter the trends or conclusions drawn here.

Figure 10 shows the instability metric, $\int |\hat{f}(k)|^2 dk$, plotted against the total preheat energy deposited and the neutron yield. The values of this metric for the same no-DPP experiments in this paper were calculated in Ampleford *et al.*¹¹ and were shown to be more stable than equivalent uncoated AR6 and AR9 experiments, demonstrating that dielectric coatings improve stability. The data show some variation in the instability metric for the co-injection shots but overall values

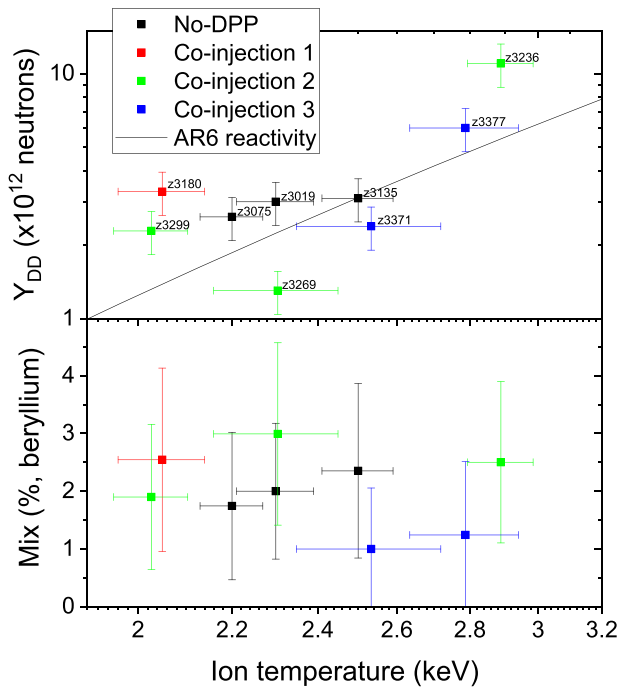


FIG. 8. Plots of the DD neutron yield vs ion temperature (top) and the percentage of Be mix material inferred to be present at stagnation as a function of ion temperature (bottom). The data used are listed in Table II. The “AR6 scaling curve” shows the DD-3He reactivity scaled to match data from AR6 MagLIF experiments.¹⁷

similar to the no-DPP values. The data appear to show some positive correlation between increased preheat energy and increased instability for the co-injection experiments, again noting that shot z3299 may have had issues with preheat coupling due to the presence of debris above the LEH foil during preheat. However, since preheat energy has a positive correlation with performance metrics such as χ , ion temperature, and neutron yield, this indicates that the effect of stability on

performance within this dataset is not a dominant effect, possibly because of the overall low levels of instability growth. Note this does not mean that instability is not impacting performance, as it is possible that the improvements to output parameters based on preheat energy deposited could have been larger had the experiments exhibited equal stability. Future work³⁸ will analyze the relationship between instability growth over a wide variety of input parameters including preheat to make more robust statistical claims about this apparent effect.

In addition to structure in the strand position, some of the images in Fig. 9 show localized regions of higher-intensity emission. Assuming this emission was coming predominantly from the fuel, these hotspots would be expected to coincide with localized regions of increased neutron production, which, ideally, would be diagnosed with an image of the neutron emission. The One-Dimensional Imager of Neutrons (ODIN)³⁹ diagnostic is capable of providing these data and was fielded on many shots in this dataset. However, the signal-to-noise ratio on this instrument was generally low. Previous work has shown that the x-ray emissivity tracks the ODIN data well and can be used as a surrogate for the purpose of identifying hotspots.³⁹ While the SCI images, as shown in Fig. 9, can provide these data, the different types of SCIs used have different sensitivities and spectral bands, and at lower energies (particularly emission around 6 keV), the observed emission can be strongly attenuated by the liner material leading to additional features in the emission profile that are due to axial variations in the liner opacity. The TIPC pinhole camera²⁹ diagnostic also provided emission images through a 1.5 mm thick Kapton-filtered pinhole that allows the absolute emission intensity to be compared across the dataset, and models suggest that this diagnostic has less sensitivity to liner attenuation, relative to the SCI diagnostics. Vertical lineouts from the TIPC images from each experiment are shown in Fig. 11. Axial intensity variations show some different morphologies across the experiments. The no-DPP and co-injection 3 experiments have a similar, single broad peak, with some variations, stretching over ~6–8 mm. Shot z3180, and to a lesser extent z3299, shows multiple peaks, which may indicate that MRT feedthrough has impacted the stagnation at various axial locations. Finally, shots z3236 and z3269 show two broad

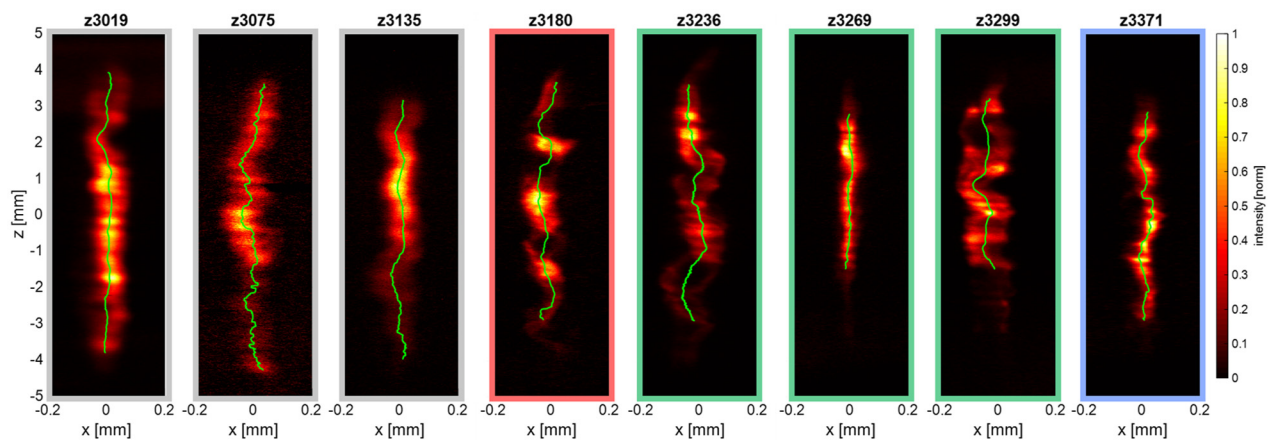


FIG. 9. Stagnation images from the SCI diagnostics fielded on different shots. The intensity is on a linear, normalized scale that varies between shots. The mean radial position of the column is plotted in green. The different border colors represent different preheat configurations using the same color scheme as used in Fig. 1 and elsewhere. The horizontal axis has been stretched to highlight structure in the columns.

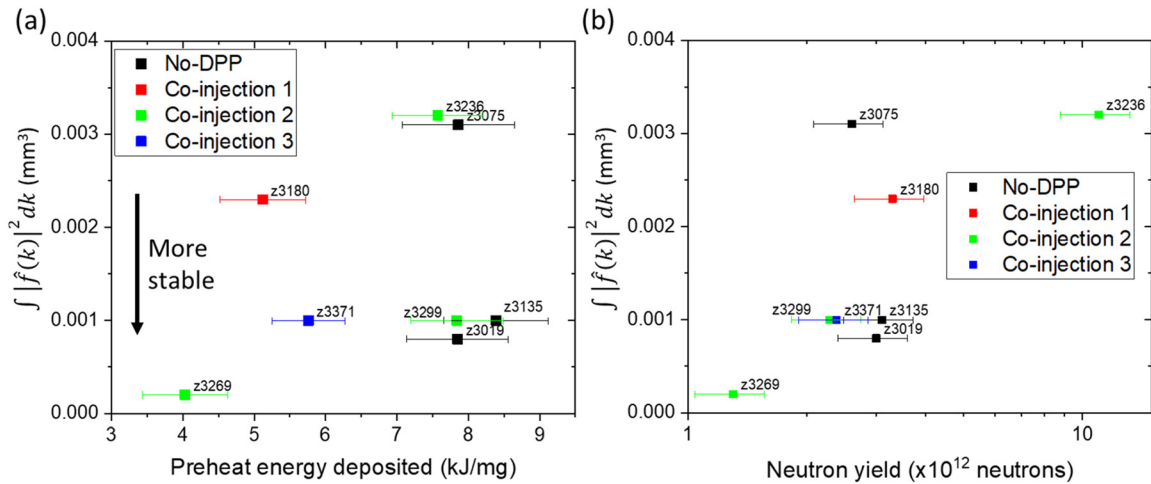


FIG. 10. Values of the instability metric as a function of (a) specific preheat energy deposited into the fuel and (b) neutron yield. By this metric, the experiments are more stable than uncoated AR6 experiments that returned values of 0.004 and 0.009 (Ref. 11) and do not show a strong correlation between the instability metric and preheat energy or neutron yield.

emission peaks each over 1.5 mm in length. Overall, while significant intensity variations are present along the axial length of the stagnation columns, with the exception of shot z3180, the emission tends to come from extended regions greater than 1 mm in length. Shot z3236, for example, has two emission peaks whose FWHM of 1.5 and 1.8 mm totals about 1/3rd of the imploding length. The remaining emission is

still at a moderate intensity, suggesting neutrons are produced along the length of the column indicating effective compression of the fuel. These observations, while qualitative, suggest that variations in the stagnation morphology are not drivers of the observed trends in neutron yield for the co-injection experiments. However, they do not suggest that the morphology is improved for co-injection vs no-DPP experiments and do not explain the relative increase in performance.

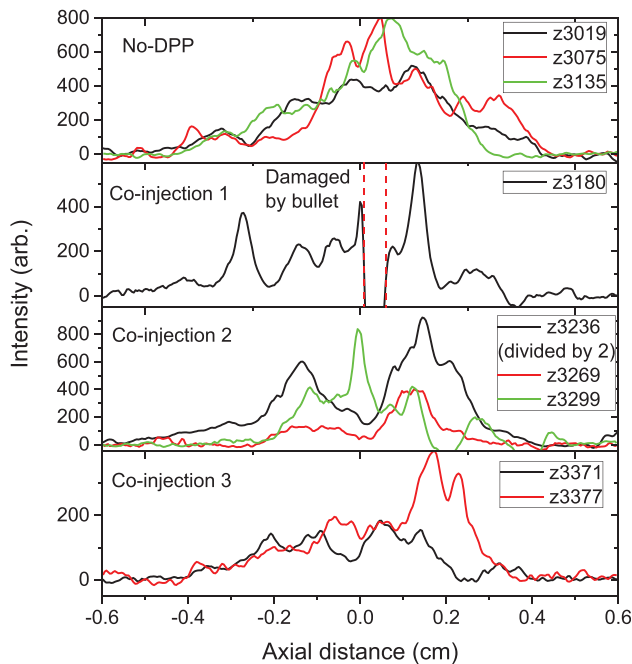


FIG. 11. Axial intensity lineouts from a 1.5 mm Kapton-filtered pinhole imager. The lineouts use the same linear intensity scale that is consistent across experiments. Shot z3180 has partial data loss due to damage on the image plate detector. The signal intensity for z3236 has been divided by two to aid comparisons.

IV. DISCUSSION

In summary, a series of laser preheat configurations have been designed and tested, which increase the laser energy coupled while reducing the amount of contaminants mixed into the fuel volume. The preheat configurations were tested on the coated AR9 MagLIF platform, which has previously produced consistent neutron yields with the “no-DPP” preheat configuration. For the co-injection preheat configurations, the neutron yields are found to increase with specific preheat energy, in line with Kraken simulations that include mix material in the fuel. The peak neutron yield of $Y_{DD} = 1.1 \times 10^{13}$ in z3236 is 3–4 times higher than for experiments using the no-DPP preheat configurations. Mix and morphology are explored as hypotheses to explain the increased peak neutron yields for the co-injection vs no-DPP preheat configurations. It is thought that the co-injection configurations may reduce mix material in the fuel by reducing the amount of beam spray and LEH foil material introduced. However, we find the mix inference from the Bayesian analysis is not sufficiently constraining to conclude whether mix is a determining factor. This points to a need to better constrain mix in MagLIF experiments. Improvements may be possible in the future by incorporating neutron imaging and information from spectroscopy into the Bayesian framework. Similarly, it was thought that the increased fuel density and preheat energies used in the co-injection configurations may reduce the stagnation convergence ratio and improve morphology. However, the stagnated plasma columns show similar morphologies across the dataset, and changes in stability do not appear to explain the trends observed based on the metrics used. We note though that the extent to which the overall

performance of the reported experiments is impacted by instability growth is not yet known. It is likely that a larger dataset with improved mix and morphology measurements will be required to resolve the differences in performance between the co-injection and no-DPP experiments and increase confidence in the observed trends. Such experiments could utilize doped materials, such as a volumetric cobalt dopant in the Beryllium liner or cushions that have recently been developed, and multiple imaging lines of sight to improve morphology quantification and incorporate more information from, e.g., spectroscopy in the Bayesian analysis.

The peak neutron yield of $Y_{DD} = 1.1 \times 10^{13}$ in shot z3236 equals the highest achieved to date in MagLIF experiments¹⁷ and demonstrates the potential benefits of using high AR liners in MagLIF. By comparison, the highest yield achieved with an uncoated AR6 Be liner with $B_z = 10$ T, and the same electrical transmission line design was $Y_{DD} = 4 \times 10^{12}$ in z3040.^{15,40} A similar neutron yield was achieved in shot z3289 with an AR6 Be liner and similar preheat parameters to z3236 but with a higher magnetic field (15 T) and more efficient transmission line design, both changes that were expected to increase the yield.¹⁷ This relatively better performance for the coated AR9 experiments reported here is as expected from 2D simulations, which, in the absence of instabilities, show that AR9 liners reach higher implosion velocities than AR6 liners and produce higher maximum neutron yields for a given feed design and applied B field. This improvement is predicated on being able to maintain sufficient liner stability during the implosion.

Whether the stability of MagLIF implosions is sufficient is a crucial question moving forward. The evidence in this paper suggests that the stability of coated AR9 liners is comparable to, or better than, uncoated AR6 liners. First, an instability metric applied to high resolution images of the stagnations reinforces the observation in Ampleford *et al.*,¹¹ that coated AR9 stagnations exhibit less variations in the radial position of the column. Second, the highest neutron yield in z3236 of 1.1×10^{13} is a factor 3.6 below the 40×10^{12} peak yield predicted by 2D Kraken simulations for a fuel without mix. This is similar to the ~factor 3 degradation observed between 2D simulations and the best-performing AR6 liner experiments,¹⁷ although the degradation mechanisms may be different between these cases.

There is the potential to further improve the performance of coated AR9 liner experiments on Z utilizing recent advances in current drive, preheat energy, and magnetic field. Since these experiments were conducted, lower inductance transmission lines and advanced magnetic field coil designs have demonstrated improved current coupling with 15 T applied magnetic fields.¹⁷ New preheat configurations that utilize cryogenic cooling to minimize the LEH foil thickness have also demonstrated significant improvements in preheat energy while mitigating LEH foil mix. Combining these capabilities with coated AR9 liners could potentially further increase the performance of future MagLIF experiments.

The scaling of MagLIF performance to higher currents is captured by similarity scaling models⁴ that prescribe the liner geometry, magnetic field, fuel density, and preheat energy required to produce a “similar” implosion at a given current and predict the resulting stagnation parameters. These models provide a way to conservatively scale the performance of MagLIF on the Z generator to future generators at higher currents. Such scaling relies on “baseline” experiments conducted on Z. Increasing the performance metrics (neutron yield and

stagnation pressure) of MagLIF experiments on Z while minimizing the required input parameters (current, laser energy, and magnetic field) will result in higher predicted performances on future generators with realistic inputs. The robustness to MRT growth and the now demonstrated higher neutron yields make the coated AR9 platform potentially interesting for demonstrating scaling to higher yields. It also motivates further development of techniques that mitigate MRT growth to enable stable, higher aspect ratio liner implosions such as novel liner materials, graded densities, and the dynamic screw pinch.^{41,42}

ACKNOWLEDGMENTS

Sandia National Laboratories is a multimission laboratory managed and operated by National Technology & Engineering Solutions of Sandia, LLC, a wholly owned subsidiary of Honeywell International Inc., for the U.S. Department of Energy’s National Nuclear Security Administration under Contract DE-NA0003525. This paper describes objective technical results and analysis. Any subjective views or opinions that might be expressed in the paper do not necessarily represent the views of the U.S. Department of Energy or the United States Government.

AUTHOR DECLARATIONS

Conflict of Interest

The authors have no conflicts to disclose.

Author Contributions

Adam James Harvey-Thompson: Formal analysis (equal); Investigation (equal); Writing – original draft (equal). **Matthias Geissel:** Conceptualization (equal); Formal analysis (equal); Investigation (equal); Methodology (equal). **William E. Lewis:** Formal analysis (equal); Methodology (equal); Writing – review & editing (equal). **David Yager-Elorriaga:** Formal analysis (equal); Methodology (equal); Writing – review & editing (equal). **Matthew Robert Weis:** Conceptualization (equal); Investigation (equal); Methodology (equal); Software (equal); Writing – review & editing (equal). **Christopher A. Jennings:** Formal analysis (equal); Investigation (equal); Methodology (equal); Software (equal). **Jeffrey Robert Fein:** Investigation (equal); Methodology (equal); Writing – review & editing (equal). **David Ampleford:** Conceptualization (equal); Formal analysis (equal); Methodology (equal); Project administration (equal); Writing – review & editing (equal). **Matthew R. Gomez:** Investigation (equal); Writing – review & editing (equal). **Eric C. Harding:** Investigation (equal); Methodology (equal). **Stephanie B. Hansen:** Investigation (equal); Methodology (equal). **David E. Bliss:** Investigation (equal); Methodology (equal). **Gordon A. Chandler:** Data curation (equal); Formal analysis (equal). **Greg S. Dunham:** Formal analysis (equal). **Ella Field:** Methodology (equal). **Benjamin Robert Galloway:** Investigation (equal). **Michael E. Glinsky:** Investigation (equal); Methodology (equal); Software (equal). **Kelly Hahn:** Data curation (equal); Formal analysis (equal). **Patrick Francis Knapp:** Investigation (equal); Methodology (equal). **Derek Lamppa:** Investigation (equal). **Larry M. Lucero:** Investigation (equal). **Michael Mangan:** Formal analysis (equal); Investigation (equal). **Reny Paguio:** Investigation (equal); Project administration (equal). **Lawrence Perea:**

Investigation (equal). **Kyle J. Peterson**: Conceptualization (equal); Project administration (equal); Software (equal). **John Porter**: Project administration (equal). **Patrick Rambo**: Investigation (equal); Methodology (equal). **Grafton Robertson**: Project administration (equal). **Gregory Rochau**: Project administration (equal); Supervision (equal). **Daniel Edward Ruiz**: Investigation (equal); Methodology (equal); Software (equal). **Carlos L. Ruiz**: Investigation (equal); Methodology (equal). **Marc-Andre Schaeuble**: Formal analysis (equal). **Jens Schwarz**: Methodology (equal). **Jonathon E. Shores**: Methodology (equal). **Daniel B. Sinars**: Project administration (equal); Supervision (equal). **Stephen A. Slutz**: Conceptualization (equal); Software (equal). **Gary Smith**: Resources (equal). **Ian Smith**: Investigation (equal); Methodology (equal). **C. S. Speas**: Resources (equal). **Kelly Whittemore**: Resources (equal). **Edmund P. Yu**: Conceptualization (equal); Software (equal).

DATA AVAILABILITY

The data that support the findings of this study are available from the corresponding author upon reasonable request.

REFERENCES

- ¹S. A. Slutz, M. C. Herrmann, R. A. Vesey, A. B. Sefkow, D. B. Sinars, D. C. Rovang, K. J. Peterson, and M. E. Cuneo, "Pulsed-power-driven cylindrical laser implosions of laser preheated fuel magnetized with an axial field," *Phys. Plasmas* **17**(5), 056303 (2010).
- ²M. R. Gomez, S. A. Slutz, A. B. Sefkow, D. B. Sinars, K. D. Hahn, S. B. Hansen, E. C. Harding, P. F. Knapp, P. F. Schmit, C. A. Jennings, T. J. Awe, M. Geissel, D. C. Rovang, G. A. Chandler, G. W. Cooper, M. E. Cuneo, A. J. Harvey-Thompson, M. C. Herrmann, M. H. Hess, O. Johns, D. C. Lamppa, M. R. Martin, R. D. McBride, K. J. Peterson, J. L. Porter, G. K. Robertson, G. A. Rochau, C. L. Ruiz, M. E. Savage, I. C. Smith, W. A. Stygar, and R. A. Vesey, "Experimental demonstration of fusion-relevant conditions in magnetized liner inertial fusion," *Phys. Rev. Lett.* **113**(15), 155003 (2014).
- ³S. A. Slutz, W. A. Stygar, M. R. Gomez, K. J. Peterson, A. B. Sefkow, D. B. Sinars, R. A. Vesey, E. M. Campbell, and R. Betti, "Scaling magnetized liner inertial fusion on Z and future pulsed-power accelerators," *Phys. Plasmas* **23**(2), 022702 (2016).
- ⁴D. E. Ruiz, P. F. Schmit, D. A. Yager-Elorriaga, M. R. Gomez, M. R. Weis, C. A. Jennings, A. J. Harvey-Thompson, P. F. Knapp, S. A. Slutz, D. J. Ampleford, K. Beckwith, and M. K. Matzen, "Exploring the parameter space of MagLIF implosions using similarity scaling. II. Current scaling," *Phys. Plasmas* **30**(3), 032708 (2023).
- ⁵D. C. Rovang, D. C. Lamppa, M. E. Cuneo, A. C. Owen, J. McKenney, D. W. Johnson, S. Radovich, R. J. Kaye, R. D. McBride, C. S. Alexander, T. J. Awe, S. A. Slutz, A. B. Sefkow, T. A. Haill, P. A. Jones, J. W. Argo, D. G. Dalton, G. K. Robertson, E. M. Waisman, D. B. Sinars, J. Meissner, M. Milhous, D. N. Nguyen, and C. H. Mielke, "Pulsed-coil magnet systems for applying uniform 10–30 T fields to centimeter-scale targets on Sandia's Z facility," *Rev. Sci. Instrum.* **85**(12), 124701 (2014).
- ⁶P. K. Rambo, I. C. Smith, J. L. Porter, M. J. Hurst, C. S. Speas, R. G. Adams, A. J. Garcia, E. Dawson, B. D. Thurston, C. Wakefield, J. W. Kellogg, M. J. Slattery, H. C. Ives, R. S. Broyles, J. A. Caird, A. C. Erlandson, J. E. Murray, W. C. Behrendt, N. D. Neilsen, and J. M. Narduzzi, "Z-Beamlet: A multikilojoule, terawatt-class laser system," *Appl. Opt.* **44**(12), 2421–2430 (2005).
- ⁷P. Rambo, J. Schwarz, M. Schollmeier, M. Geissel, I. Smith, M. Kimmel, C. Speas, J. Shores, D. Armstrong, J. Bellum, E. Field, D. Kletecka, and J. Porter, "Sandia's Z-Backlighter laser facility," in *Laser-Induced Damage in Optical Materials* (SPIE, 2016), pp. 103–118.
- ⁸M. E. Savage, K. R. LeChien, M. R. Lopez, B. S. Stoltzfus, W. A. Stygar, D. S. Artery, J. A. Lott, and P. A. Corcoran, "Status of the Z pulsed power driver," in *IEEE Pulsed Power Conference* (IEEE, 2011), pp. 983–990.
- ⁹D. V. Rose, D. R. Welch, E. A. Madrid, C. L. Miller, R. E. Clark, W. A. Stygar, M. E. Savage, G. A. Rochau, J. E. Bailey, T. J. Nash, M. E. Seiford, K. W. Struve, P. A. Corcoran, and B. A. Whitney, "Three-dimensional electromagnetic model of the pulsed-power Z-pinch accelerator," *Phys. Rev. Spec. Top. Accel. Beams* **13**(1), 010402 (2010).
- ¹⁰I. R. Lindemuth and R. C. Kirkpatrick, *Nucl. Fusion* **23**, 263 (1983).
- ¹¹D. J. Ampleford, D. A. Yager-Elorriaga, C. A. Jennings, E. C. Harding, M. R. Gomez, A. J. Harvey-Thompson, T. J. Awe, G. A. Chandler, G. S. Dunham, M. Geissel, K. D. Hahn, S. B. Hansen, P. F. Knapp, D. C. Lamppa, W. E. Lewis, L. Lucero, M. Mangan, R. Paguio, L. Perea, G. A. Robertson, C. L. Ruiz, D. E. Ruiz, P. F. Schmit, S. A. Slutz, G. E. Smith, I. C. Smith, C. S. Speas, T. J. Webb, M. R. Weis, K. Whittemore, E. P. Yu, R. D. McBride, K. J. Peterson, B. M. Jones, G. A. Rochau, and D. B. Sinars, "Controlling morphology and improving reproducibility of magnetized liner inertial fusion experiments," *Phys. Plasmas* **31**(2), 022703 (2024).
- ¹²K. J. Peterson, T. J. Awe, E. P. Yu, D. B. Sinars, E. S. Field, M. E. Cuneo, M. C. Herrmann, M. Savage, D. Schroen, K. Tomlinson, and C. Nakhleh, "Electrothermal instability mitigation by using thick dielectric coatings on magnetically imploded conductors," *Phys. Rev. Lett.* **112**(13), 135002 (2014).
- ¹³T. J. Awe, K. J. Peterson, E. P. Yu, R. D. McBride, D. B. Sinars, M. R. Gomez, C. A. Jennings, M. R. Martin, S. E. Rosenthal, D. G. Schroen, A. B. Sefkow, S. A. Slutz, K. Tomlinson, and R. A. Vesey, "Experimental demonstration of the stabilizing effect of dielectric coatings on magnetically accelerated imploding metallic liners," *Phys. Rev. Lett.* **116**(6), 065001 (2016).
- ¹⁴A. J. Harvey-Thompson, M. R. Weis, E. C. Harding, M. Geissel, D. J. Ampleford, G. A. Chandler, J. R. Fein, M. E. Glinsky, M. R. Gomez, K. D. Hahn, S. B. Hansen, C. A. Jennings, P. F. Knapp, R. R. Paguio, L. Perea, K. J. Peterson, J. L. Porter, P. K. Rambo, G. K. Robertson, G. A. Rochau, D. E. Ruiz, J. Schwarz, J. E. Shores, D. B. Sinars, S. A. Slutz, G. E. Smith, I. C. Smith, C. S. Speas, and K. Whittemore, "Diagnosing and mitigating laser preheat induced mix in MagLIF," *Phys. Plasmas* **25**(11), 112705 (2018).
- ¹⁵A. J. Harvey-Thompson, M. Geissel, C. A. Jennings, M. R. Weis, M. R. Gomez, J. R. Fein, D. J. Ampleford, G. A. Chandler, M. E. Glinsky, K. D. Hahn, S. B. Hansen, E. C. Harding, P. F. Knapp, R. R. Paguio, L. Perea, K. J. Peterson, J. L. Porter, P. K. Rambo, G. K. Robertson, G. A. Rochau, C. L. Ruiz, J. Schwarz, J. E. Shores, D. B. Sinars, S. A. Slutz, G. E. Smith, I. C. Smith, C. S. Speas, K. Whittemore, and D. Woodbury, "Constraining preheat energy deposition in MagLIF experiments with multi-frame shadowgraphy," *Phys. Plasmas* **26**(3), 032707 (2019).
- ¹⁶S. A. Slutz, M. R. Gomez, S. B. Hansen, E. C. Harding, B. T. Hutsel, P. F. Knapp, D. C. Lamppa, T. J. Awe, D. J. Ampleford, D. E. Bliss, G. A. Chandler, M. E. Cuneo, M. Geissel, M. E. Glinsky, A. J. Harvey-Thompson, M. H. Hess, C. A. Jennings, B. Jones, G. R. Laity, M. R. Martin, K. J. Peterson, J. L. Porter, P. K. Rambo, G. A. Rochau, C. L. Ruiz, M. E. Savage, J. Schwarz, P. F. Schmit, G. Shipley, D. B. Sinars, I. C. Smith, R. A. Vesey, and M. R. Weis, "Enhancing performance of magnetized liner inertial fusion at the Z facility," *Phys. Plasmas* **25**(11), 112706 (2018).
- ¹⁷M. R. Gomez, S. A. Slutz, C. A. Jennings, D. J. Ampleford, M. R. Weis, C. E. Myers, D. A. Yager-Elorriaga, K. D. Hahn, S. B. Hansen, E. C. Harding, A. J. Harvey-Thompson, D. C. Lamppa, M. Mangan, P. F. Knapp, T. J. Awe, G. A. Chandler, G. W. Cooper, J. R. Fein, M. Geissel, M. E. Glinsky, W. E. Lewis, C. L. Ruiz, D. E. Ruiz, M. E. Savage, P. F. Schmit, I. C. Smith, J. D. Stryon, J. L. Porter, B. Jones, T. R. Mattsson, K. J. Peterson, G. A. Rochau, and D. B. Sinars, "Performance scaling in magnetized liner inertial fusion experiments," *Phys. Rev. Lett.* **125**(15), 155002 (2020).
- ¹⁸R. Betti, P. Y. Chang, B. K. Spears, K. S. Anderson, J. Edwards, M. Fatenejad, J. D. Lindl, R. L. McCrory, R. Nora, and D. Shvarts, "Thermonuclear ignition in inertial confinement fusion and comparison with magnetic confinement," *Phys. Plasmas* **17**(5), 058102 (2010).
- ¹⁹P. F. Knapp, M. E. Glinsky, M. A. Schaeuble, C. A. Jennings, M. Evans, J. Gunning, T. J. Awe, G. A. Chandler, M. Geissel, M. R. Gomez, K. D. Hahn, S. B. Hansen, E. C. Harding, A. J. Harvey-Thompson, S. Humane, B. T. Klein, M. Mangan, T. Nagayama, A. J. Porwitzky, D. E. Ruiz, P. F. Schmit, S. A. Slutz, I. C. Smith, M. R. Weis, D. A. Yager-Elorriaga, D. J. Ampleford, K. Beckwith, T. R. Mattsson, K. J. Peterson, and D. B. Sinars, "Estimation of stagnation performance metrics in magnetized liner inertial fusion experiments using Bayesian data assimilation," *Phys. Plasmas* **29**(5), 052711 (2022).

- ²⁰A. J. Harvey-Thompson, M. Geissel, J. A. Crabtree, M. R. Weis, M. R. Gomez, J. R. Fein, W. E. Lewis, D. J. Ampleford, T. J. Awe, G. A. Chandler, B. R. Galloway, S. B. Hansen, J. Hanson, E. C. Harding, C. A. Jennings, M. Kimmel, P. F. Knapp, M. A. Mangan, A. Maurer, R. R. Paguio, L. Perea, K. J. Peterson, J. L. Porter, P. K. Rambo, G. K. Robertson, G. A. Rochau, D. E. Ruiz, J. E. Shores, S. A. Slutz, G. E. Smith, I. C. Smith, C. S. Speas, D. A. Yager-Elorriaga, and A. York, "Demonstration of improved laser preheat with a cryogenically cooled magnetized liner inertial fusion platform," *Rev. Sci. Instrum.* **94**(5), 053506 (2023).
- ²¹P. F. Schmit and D. E. Ruiz, "A conservative approach to scaling magneto-inertial fusion concepts to larger pulsed-power drivers," *Phys. Plasmas* **27**(6), 062707 (2020).
- ²²A. B. Sefkow, S. A. Slutz, J. M. Koning, M. M. Marinak, K. J. Peterson, D. B. Sinars, and R. A. Vesey, "Design of magnetized liner inertial fusion experiments using the Z facility," *Phys. Plasmas* **21**(7), 072711 (2014).
- ²³M. M. Marinak, R. E. Tipton, O. L. Landen, T. J. Murphy, P. Amendt, S. W. Haan, S. P. Hatchett, C. J. Keane, R. McEachern, and R. Wallace, "Three-dimensional simulations of Nova high growth factor capsule implosion experiments," *Phys. Plasmas* **3**(5), 2070–2076 (1996).
- ²⁴J. Schwarz, P. Rambo, M. Geissel, A. Edens, I. Smith, E. Brambrink, M. Kimmel, and B. Atherton, "Activation of the Z-petawatt laser at Sandia National Laboratories," *J. Phys. Conf. Ser.* **112**(3), 032020 (2008).
- ²⁵M. Geissel, A. J. Harvey-Thompson, T. J. Awe, D. E. Bliss, M. E. Glinsky, M. R. Gomez, E. Harding, S. B. Hansen, C. Jennings, M. W. Kimmel, P. Knapp, S. M. Lewis, K. Peterson, M. Schollmeier, J. Schwarz, J. E. Shores, S. A. Slutz, D. B. Sinars, I. C. Smith, C. S. Speas, R. A. Vesey, M. R. Weis, and J. L. Porter, "Minimizing scatter-losses during pre-heat for magneto-inertial fusion targets," *Phys. Plasmas* **25**(2), 022706 (2018).
- ²⁶P. F. Knapp, M. R. Gomez, S. B. Hansen, M. E. Glinsky, C. A. Jennings, S. A. Slutz, E. C. Harding, K. D. Hahn, M. R. Weis, M. Evans, M. R. Martin, A. J. Harvey-Thompson, M. Geissel, I. C. Smith, D. E. Ruiz, K. J. Peterson, B. M. Jones, J. Schwarz, G. A. Rochau, D. B. Sinars, R. D. McBride, and P.-A. Gourdain, "Origins and effects of mix on magnetized liner inertial fusion target performance," *Phys. Plasmas* **26**(1), 012704 (2019).
- ²⁷S. B. Hansen, M. R. Gomez, A. B. Sefkow, S. A. Slutz, D. B. Sinars, K. D. Hahn, E. C. Harding, P. F. Knapp, P. F. Schmit, T. J. Awe, R. D. McBride, C. A. Jennings, M. Geissel, A. J. Harvey-Thompson, K. J. Peterson, D. C. Rovang, G. A. Chandler, G. W. Cooper, M. E. Cuneo, M. C. Herrmann, M. H. Hess, O. Johns, D. C. Lamppa, M. R. Martin, J. L. Porter, G. K. Robertson, G. A. Rochau, C. L. Ruiz, M. E. Savage, I. C. Smith, W. A. Stygar, R. A. Vesey, B. E. Blue, D. Ryutov, D. G. Schroen, and K. Tomlinson, "Diagnosing magnetized liner inertial fusion experiments on Z," *Phys. Plasmas* **22**(5), 056313 (2015).
- ²⁸E. C. Harding, T. Ao, J. E. Bailey, G. Loisel, D. B. Sinars, M. Geissel, G. A. Rochau, and I. C. Smith, "Analysis and implementation of a space resolving spherical crystal spectrometer for x-ray Thomson scattering experiments," *Rev. Sci. Instrum.* **86**(4), 043504 (2015).
- ²⁹L. A. McPherson, D. J. Ampleford, C. A. Coverdale, J. W. Argo, A. C. Owen, and D. M. Jaramillo, "High energy X-ray pinhole imaging at the Z facility," *Rev. Sci. Instrum.* **87**(6), 063502 (2016).
- ³⁰E. C. Harding, G. K. Robertson, G. S. Dunham, M. R. Gomez, J. R. Fein, P. F. Knapp, A. J. Harvey-Thompson, C. S. Speas, D. J. Ampleford, G. A. Rochau, R. Doron, and Y. Maron, "X-ray self-emission imaging with spherically bent Bragg crystals on the Z-machine," *Rev. Sci. Instrum.* **94**(8), 083509 (2023).
- ³¹C. L. Ruiz, D. L. Fehl, G. A. Chandler, G. Cooper, B. Jones, J. D. Styron, and J. Torres, "Multichannel, triaxial, neutron time-of-flight diagnostic for experiments at the Z facility," *Phys. Rev. Accel. Beams* **23**(2), 020401 (2020).
- ³²G. A. Chandler, C. L. Ruiz, G. W. Cooper, J. A. Torres, M. A. Mangan, G. M. Whitlow, D. J. Ampleford, M. C. Jones, R. A. Buckles, K. J. Moy, I. Garza, M. Staska, A. Wolverton, and B. Davis, "Neutron time-of-flight detectors (nTOF) used at Sandia's Z-Machine," *Rev. Sci. Instrum.* **93**(11), 113531 (2022).
- ³³W. E. Lewis, P. F. Knapp, S. A. Slutz, P. F. Schmit, G. A. Chandler, M. R. Gomez, A. J. Harvey-Thompson, M. A. Mangan, D. J. Ampleford, and K. Beckwith, "Deep-learning-enabled Bayesian inference of fuel magnetization in magnetized liner inertial fusion," *Phys. Plasmas* **28**(9), 092701 (2021).
- ³⁴J. P. Chittenden, S. V. Lebedev, C. A. Jennings, S. N. Bland, and A. Ciardi, "X-ray generation mechanisms in three-dimensional simulations of wire array Z-pinches," *Plasma Phys. Controlled Fusion* **46**(12B), B457 (2004).
- ³⁵A. Ciardi, S. V. Lebedev, A. Frank, E. G. Blackman, J. P. Chittenden, C. J. Jennings, D. J. Ampleford, S. N. Bland, S. C. Bott, J. Rapley, G. N. Hall, F. A. Suzuki-Vidal, A. Marocchino, T. Lery, and C. Stehle, "The evolution of magnetic tower jets in the laboratory," *Phys. Plasmas* **14**(5), 056501 (2007).
- ³⁶D. E. Ruiz, P. F. Schmit, D. A. Yager-Elorriaga, C. A. Jennings, and K. Beckwith, "Exploring the parameter space of MagLIF implosions using similarity scaling. I. Theoretical framework," *Phys. Plasmas* **30**(3), 032707 (2023).
- ³⁷R. D. McBride and S. A. Slutz, "A semi-analytic model of magnetized liner inertial fusion," *Phys. Plasmas* **22**(5), 052708 (2015).
- ³⁸W. E. Lewis, "Mining experimental magnetized liner inertial fusion stagnation images: Trends in stagnation morphology," (unpublished).
- ³⁹D. J. Ampleford, C. L. Ruiz, D. N. Fittinghoff, J. D. Vaughan, K. Hahn, B. Lahmann, M. Gatu-Johnson, J. Frenje, R. Petrasso, C. R. Ball, A. J. Maurer, P. F. Knapp, A. J. Harvey-Thompson, J. Fisher, P. Alberto, J. A. Torres, G. Cooper, B. Jones, G. A. Rochau, and M. J. May, "One dimensional imager of neutrons on the Z machine," *Rev. Sci. Instrum.* **89**(10), 101132 (2018).
- ⁴⁰M. R. Gomez, S. A. Slutz, P. F. Knapp, K. D. Hahn, M. R. Weis, E. C. Harding, M. Geissel, J. R. Fein, M. E. Glinsky, S. B. Hansen, A. J. Harvey-Thompson, C. A. Jennings, I. C. Smith, D. Woodbury, D. J. Ampleford, T. J. Awe, G. A. Chandler, M. H. Hess, D. C. Lamppa, C. E. Myers, C. L. Ruiz, A. B. Sefkow, J. Schwarz, D. A. Yager-Elorriaga, B. Jones, J. L. Porter, K. J. Peterson, R. D. McBride, G. A. Rochau, and D. B. Sinars, "Assessing stagnation conditions and identifying trends in magnetized liner inertial fusion," *IEEE Trans. Plasma Sci.* **47**(5), 2081–2101 (2019).
- ⁴¹P. F. Schmit, A. L. Velikovich, R. D. McBride, and G. K. Robertson, "Controlling Rayleigh-Taylor instabilities in magnetically driven solid metal shells by means of a dynamic screw pinch," *Phys. Rev. Lett.* **117**(20), 205001 (2016).
- ⁴²G. A. Shipley, C. A. Jennings, and P. F. Schmit, "Design of dynamic screw pinch experiments for magnetized liner inertial fusion," *Phys. Plasmas* **26**(10), 102702 (2019).